



Failure characteristics of rock-like materials with single flaws under uniaxial compression

Cheng Zhao^{1,2} · Jialun Niu¹ · Qingzhao Zhang¹  · Chunfeng Zhao¹ · Yimeng Zhou¹

Received: 12 March 2018 / Accepted: 24 August 2018 / Published online: 12 September 2018
© Springer-Verlag GmbH Germany, part of Springer Nature 2018

Abstract

A uniaxial compression test was conducted with a servo loading apparatus to study the failure of a rock-like specimen with a pre-existing single flaw. The evolution of cracks was monitored with digital image correlation technology and simulated with the expanded distinct element method based on the strain strength criterion. The concentration and evolution of the principal strain field were found to be consistent with the initiation, propagation, and coalescence of cracks. As the inclination angle increased, the position of the maximum principal strain concentration changed from within the flaw to the flaw tips, and the distribution of the horizontal displacement field changed from symmetric to antisymmetric. The initiation stress and peak strength were affected by the inclination angle; they were minimum when the inclination angle was 60°. As the inclination angle increased, the failure mode of the specimens transformed from mostly tensile failure to mostly shear failure.

Keywords Single flaw · Uniaxial compression · Digital image correlation method (DIC) · Strain field · Expanded distinct element method (EDEM)

Introduction

Engineering rock mass contains a large number of discontinuities at various scales, which are the result of a variety of geological processes. A multitude of construction projects have shown that the failure behaviours of rock mass are heavily controlled by the pre-existing discontinuities or cracks. Accordingly, the investigation of fracture behaviours plays an

important role in understanding the failure mechanism of the rock mass and predicting the unstable failure of jointed rock engineering. A thorough understanding of the failure processes in rock is crucial to geological engineering design and implementation, including rock slope stability analysis (Zheng et al. 2018), tunnel support design (Guo et al. 2016), foundation safety and stability (Jia et al. 2018), and fluid flow prediction in rock mass (Wong and Einstein 2009a; Gui et al. 2017).

The cracking mechanisms of rock have been studied experimentally on rock-like materials or rock materials. Rock-like materials have been widely used in experimental study since the flaws are easy to fabricate. The first experimental study on rock-like specimens that contained flaws under uniaxial compression was conducted by Brace and Bombolakis (1963). Since then, many studies have examined the fracture processes of pre-cracked rock-like materials under compression. Experimental studies have been performed on many different types of rock-like materials, including glass (Hoek and Bieniawski 1965; Bieniawski 1967), Columbia Resin 39 (Brace and Bombolakis 1963; Horii and Nemat-Nasser 1985), polymethyl methacrylate (Petit and Barquins 1988; Chaker and Barquins 1996), cement mortar (Cao et al. 2015), sandstone-like composite material (Wong and Chau 1998; Wong et al. 2001), and gypsum (Reyes and Einstein 1991; Shen et al. 1995; Bobet and Einstein 1998; Sagong

✉ Qingzhao Zhang
zhangqingzhao@tongji.edu.cn

Cheng Zhao
zhaocheng@tongji.edu.cn

Jialun Niu
1610245@tongji.edu.cn

Chunfeng Zhao
tjzhchf@sohu.com

Yimeng Zhou
zhouyimeng52@163.com

¹ Department of Geotechnical Engineering and Key Laboratory of Geotechnical and Underground Engineering of Ministry of Education, Tongji University, Shanghai, China

² College of Engineering, Tibet University, Lhasa, China

and Bobet 2002; Wong and Einstein 2006, 2009a, b). To investigate the initiation, propagation, and coalescence behaviours of crack in real rock materials, some experiments on rock such as granite (Basu et al. 2013; Liang et al. 2016; Zhao and He 2017), marble (Wong and Einstein 2009a, b; Zou and Wong 2014), sandstone (Yang et al. 2016, 2017), and mudstone (Hu et al. 2017) have also been conducted. Such rock-like materials and real rock materials have common characteristics for crack evolution, but also differences caused by the material properties, loading method, and specimen geometry.

Some experimental investigations observed cracks at the macroscale by choosing finite stage points during crack growth. These observations were static, in contrast with the continuous and dynamic evolution of cracks. Recently, advances in observation technology have allowed for the initiation, propagation, and coalescence to be observed with high-speed cameras (Wong and Einstein 2009a; Lin and Labuz 2013; Morgan et al. 2013; Tarokh et al. 2016). The digital image correlation (DIC) method is an optical technique for full-field and non-contact measurement of the deformation and strain of a specimen. Comprehensive dynamic observation of the crack propagation in specimens can be conducted from the microscale to the macroscale. In addition, real-time records can be obtained throughout the test process from the strain field around the cracks to create strain distribution contours, which makes it easier to observe and describe the crack propagation process.

Along with experimental studies, numerical simulations have often been applied to investigate the crack growth mechanism. Different numerical methods include the finite element method (FEM) (Huang et al. 2000; Tang et al. 2001; Agwai et al. 2011), boundary element method (BEM), bonded-particle model (BPM) (Zhang and Wong 2012, 2014; Zhang et al. 2015), numerical manifold method (NMM) (Wu and Wong 2013; Wu et al. 2017), displacement discontinuity method (DDM), and discrete element method (DEM). The DEM was developed by Cundall and Strack (1979) and is a numerical modelling method that explicitly considers individual particles and their mutual interactions in a granular assembly. The DEM can automatically identify the new contact generated by the calculation process. Vesga et al. (2008) used the DEM to simulate the cracking process in brittle clay specimens and revealed good agreement with the experimental results. Jiang et al. (2014) simulated the deformation and evolution of cracks in a fractured rock mass. Gui et al. (2016, 2017) simulated the fracturing processes in rock dynamic tests and the effect of non-banded openings by Universal Distinct Element Code (UDEC), which was implemented with a cohesive fracture model that combines tension, compression, and shear material behaviours. Jiang et al. (2009) developed an expanded distinct element method (EDEM) based on UDEC to solve the problem of the initiation and propagation path of macroscopic cracks. The approach was applied to the simulation of the crack initiation and

propagation due to the shear and tension failures in a matrix of rock blocks.

With the updating of test equipment and numerical methods, a variety of microscopic studies on cracking processes have been conducted experimentally and numerically. The cracking mechanisms based on laboratory experimental studies were identified by high-speed video observation, scanning electron microscopy, acoustic emission, and computed tomography scanning approaches (Wong and Einstein 2009a, b; Yang and Jing 2011; Lin and Labuz 2013; Zhao et al. 2017, 2018b; Fan et al. 2017). Zhang and Wong (2012, 2014) used a parallel bond model to numerically simulate the cracking process in rock-like material containing a single flaw and analyse the parallel bond forces and displacement fields at a micro level. Wu et al. (2017) investigated the micro mechanisms underlying rock macroscopic response and cracking processes by the NMM based on microscopic mechanics.

However, due to the experimental and numerical limitations, as well as the complexity of rock texture, fabric, and mineral composition, the cracking processes still need to be observed and assessed more comprehensively. There are difficulties in directly measuring and visualizing the underlying stress and strain fields. To contribute to this field of research, this paper aims to increase the understanding of the cracking mechanisms in brittle material by recording and characterizing the full-field strain and displacement, and numerically analysing the failure behaviours with strain strength criterion. By adopting the DIC method, this study effectively captured the strain and displacement distributions during the entire high-speed cracking process. The concentration and evolution of strain field in micro perspective were connected with the initiation position and propagation trajectories of macroscopic cracks. Additionally, by adopting the strain strength criterion based on DIC measurement (Zhao et al. 2017), this study obtained the quantitative analysis results of the tensile and shear behaviours of cracks.

In this study, several sets of rock-like gypsum specimens contained single flaws at different inclination angles were loaded to failure in uniaxial compression tests. Based on the DIC method, the distribution and evolution of principal strain field and horizontal displacement field during the cracking process were quantitatively recorded by analysing the movement of speckles sprayed on the specimens. Moreover, the damage evolution and cracking behaviours of flawed specimens were studied microscopically according to the concentration phenomenon of principal strain and horizontal displacement. In addition, the tensile and shear behaviours of cracks, as well as initiation stress and peak strength in different flawed specimens were numerically investigated with the EDEM. The findings of this study are of fundamental importance to understand the cracking mechanism in rock engineering applications, such as slopes, tunnels, and foundations.

Experimental setup and apparatus

Specimen preparation

Interpreting the experimental results of real rocks is typically complicated because of the variability of the specimens (Ashby and Hallam 1986). To resolve this problem, the MIT rock mechanics group has used moulded gypsum for many years to study the initiation, propagation, and coalescence of rock cracks (Reyes and Einstein 1991; Shen et al. 1995; Bobet and Einstein 1998; Sagong and Bobet 2002; Wong and Einstein 2006, 2009a, b). Moulded gypsum has advantages in specimen preparation, repeatability of experimental results, and comparison with considerable test results (Sagong and Bobet 2002). Moulded gypsum is brittle with high strength and a large ratio between tension and compression, and it can be considered as a rock-like material (Bobet and Einstein 1998). In this study, laboratory moulded gypsum specimens made from a mixture of gypsum, water, and retarder with proportions of 1:0.2:0.005 were used to simulate rock material. Zhao et al. (2017, 2018b) has used this kind of rock-like specimen to study the cracking processes and failure mechanism. The experimental results indicated that they were able to simulate the deformation behaviours of natural rock very well.

Flaws were created by inserting an aluminium shim into a slot in the mould template and removing it during curing, as shown in Fig. 1. Different flaw angles (α) of 15°, 30°, 45°, 60°, and 75° were induced to investigate the effect of flaw geometry on the crack evolution. Specimens containing different flaw angles were loaded under the same experimental conditions until failure. In order to prevent the boundary conditions of the specimens from affecting the experimental results, the position of the pre-existing flaw was placed as far as possible from the side boundaries of the specimen. The effects of the ratio of flaw size to specimen size on cracking mechanism have been studied comprehensively (Yang and Jing 2011; Zhang et al. 2015). Based on the statistical results of many past laboratory tests collected by Zhang et al. (2015), a constant flaw length of 14 mm was set in our uniaxial loading tests.

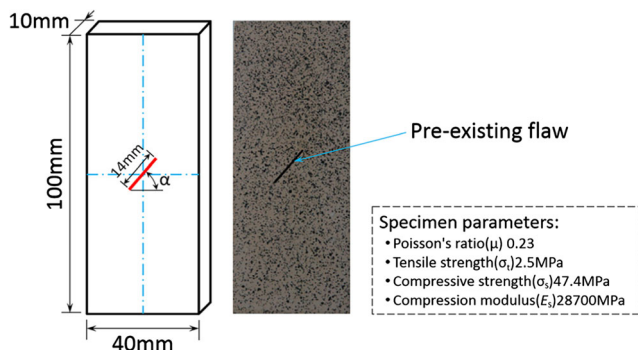


Fig. 1 Specimen prepared with a random pattern

The fixed template laid on a platform had internal dimensions of 100 mm high, 40 mm wide, and 10 mm thick (see Fig. 1). The plaster and half of the prepared water were placed into a container and stirred evenly. Then, the rest of the water was slowly poured into the container and stirred evenly. Meanwhile, oil was carefully daubed on the inner wall of the fixed template. No additional water was added once the slurry slightly overflowed from the template. The template was vibrated manually to eliminate internal air after even mixing, and the slurry that overflowed from the template was cleaned up. While the surface of the specimen remained horizontal, paper prepared with the flaw location was mounted on the surface. Then, the aluminium shim was inserted into the pre-existing slot. The fixed template was removed and the aluminium shim was drawn out 15–20 min later. Black speckles were sprayed with a random distribution on the specimen surface 12 h later. To obtain reliable experimental results, the specimen preparation was strictly controlled.

Loading apparatus

Uniaxial compression tests were performed on a Wykeham Farrance WF-5562s loading machine under load control. The average loading rate was approximately 0.002 kN/s, and the time from the beginning of loading to failure was approximately 25–30 min. Figure 2 shows the setup of the apparatus. A load cell of 5 kN was placed below the lower loading platen to measure the applied load. To reduce the friction between the specimen and loading platens, two pieces of Teflon sheets daubed with butter on the surface were inserted. All specimens were loaded until either the flaw coalesced or the specimen failed, which was identified by a drop in the applied load. All of the loading and displacement records were transferred and stored in an IBM PC through a KYOWAUC A M-5B data

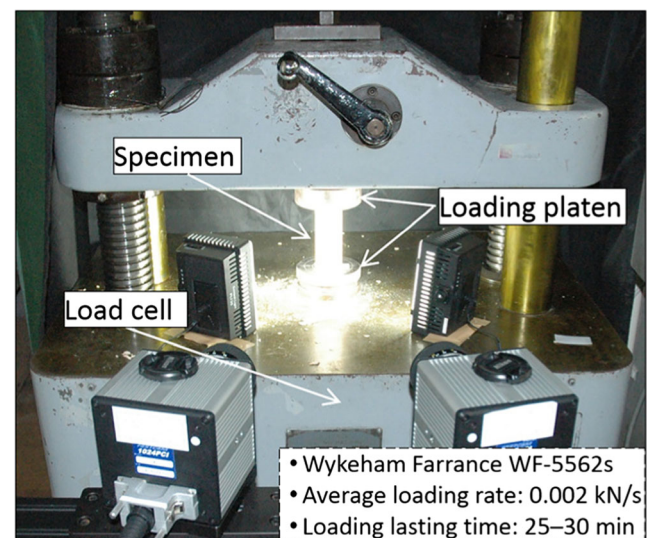


Fig. 2 Loading apparatus

logger. There was no local failure observed in any specimen. Thus, the specimen boundaries had no effect on the experimental results.

Digital image correlation (DIC) method

The DIC method is an optical technique for full-field and non-contact measurements of the deformations and strains of the components and materials. The 2D DIC system is typically sufficient for plane strain measurement. However, an artificial material was used in this study. A slight out-of-plane displacement was likely to be obtained, which would have a strong influence on the precision of results from a 2D DIC system (Huang et al. 1990). Considering these factors, a 3D DIC system was employed in the present study because of its high precision (Zhao et al. 2013, 2017, 2018a, b).

The system uses two high-resolution digital cameras to record surface changes in the specimen as it deforms. The recorded images were correlated with the correlation technique, which allowed for object contours and surface displacements to be matched with high local resolution. The movement of object points on the surface was calculated with subpixel accuracy on a plane corresponding to the initial plane. The simultaneous observation from different directions allowed for the 3D movement of each object point to be calculated. As shown in Fig. 3, two high-speed cameras were placed at a centre distance of 600 mm from the specimen, and the distance between cameras was 300 mm. Figure 4 shows a schematic of this measurement system, which consisted of specimen, cameras, and analysis system. The shutter speed of the cameras was 1/1000 s, and images were taken at approximately 0.15 mm/pixel. Two white light-emitting diode (LED) lamps were installed in front of the specimen to maintain a stable level of brightness on the specimen surface.

The speckle pattern on the specimen surface was essential because it permitted the Vic 3D software to identify and calculate the displacement and strain. First, each specimen was

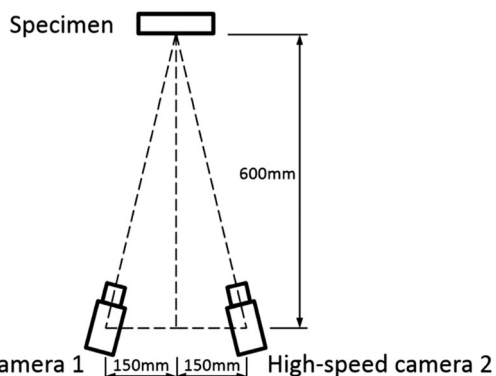


Fig. 3 Positions of the cameras and specimen

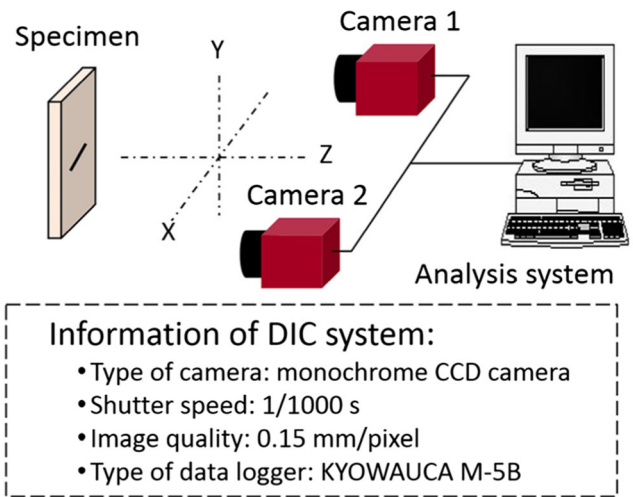


Fig. 4 Schematic diagram of the DIC system

cleaned with a degreaser, and white base paint was sprayed on the specimen surface to form a thin uniform background. After the base colour dried, a speckle pattern of black was sprayed on the same face to form a random pattern covering approximately 50% of the surface. The speckles needed to be the same size because they had the function of serving as a benchmark during the calibration of the system. Differences between patterns could be calculated by correlating all pixels of the reference image and any deformation image to generate the strain distribution. During the calibration procedure, the plate was moved towards the cameras, away from the cameras, and tilted and rotated approximately 15 times. This process provided the software with enough information for calibration.

With this method, deformations of the artificial rock-like specimens with single flaws under uniaxial compression were measured. The experimental setup is shown in Fig. 5. All specimens had the dimensions of 100 mm high, 40 mm wide, and 10 mm thick. Different specimens with different flaw

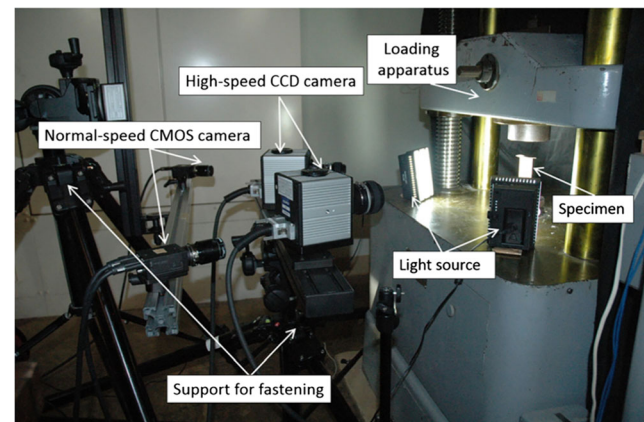


Fig. 5 Experimental setup using the 3D DIC method

angles of 15°, 30°, 45°, 60°, and 75° were tested and calculated.

Evolution of the principal strain field

Under gradually increasing uniaxial compression, the entire failure process of each specimen was observed, and a large amount of data was recorded (obtained in 0.1 s per group). The data at eight different representative time were selected from each tested specimen containing flaws at different angles. These were transformed into strain contours to show the distribution of the strain fields and changes during different stages of the crack evolution. The strain contours indicated the crack evolution from pre-existing flaws at angles α of 15°, 30°, 45°, 60°, and 75°. Among these pictures, the principal strain was chosen for data acquisition and image processing, and the range of principal strain values represented by different colours was given on the side.

Figure 6 shows the specimen with an inclination angle of 45°. The first picture (0) shows the initial state of the principal strain field before loading, where the x and y coordinates of every point were recorded as reference benchmarks to compare the principal strain changes throughout the loading process. Thus, the accumulated principal strain distribution around the flaw was acquired during the test.

When the stress increased to 78.37% of the maximum stress, as shown in picture (1) of Fig. 6, the principal strain field clearly changed around the flaw at a small scale. The principal strain was larger around the flaw tips than around other parts of the specimen, which implies that these positions represented crack initiation. The principal strain concentration indicated that the flaw entered the pre-initiation stage, but no obvious cracks were visible in the specimen.

The distribution of the principal strain fields when the load increased to 89.40% is shown in picture (2) of Fig. 6. At this point, newly generated cracks propagating from the initial flaw could be observed on the specimen surface. The principal strain field extended parallel to the loading direction, and a small principal strain field reached the region close to the

upper and lower boundaries of the specimen. This finding indicates the direction of crack propagation at a macroscale.

When the stress increased to the peak, a larger principal strain was generated near the upper and lower boundaries of the specimen, which indicated the end of crack propagation, and larger cracks could be observed on the specimen surface. As the load continued to increase, cracks coalesced between the upper and lower boundaries, which eventually led to failure of the specimen.

Principal strain fields of specimens with flaws at different inclination angles

Figure 7 compares the principal strain fields of specimens having flaws at different inclination angles. The evolutions of the principal strain fields were significantly localized in different specimens. At the beginning of loading, the maximum principal strain was concentrated around the flaw, and a localized anti-symmetric principal strain zone formed in the upper and lower regions of the flaw. With increasing load, the localized principal strain zone gradually extended along the loading direction to the upper and lower interfaces of specimen, which indicates the expansion path of the macroscopic crack. The coloured speckles at the bottom of the specimen with an inclination angle of 75° were caused by peeling at the specimen surface but had little effect on the evolution of the strain field.

There were many differences during crack initiation and propagation. With an increasing flaw angle, the position of the maximum principal strain concentration changed, which means that the position of crack initiation changed. When the angle was small (e.g., 15° and 30°), the maximum principal strain was inside the flaw tips. As the angle increased (e.g., 60° and 75°), the principal strain concentration zones gradually moved to the flaw tips. In addition, as the flaw angle increased, the angle between the direction of principal strain field extension and the direction of the flaw decreased gradually from approximately perpendicular to approximately collinear.

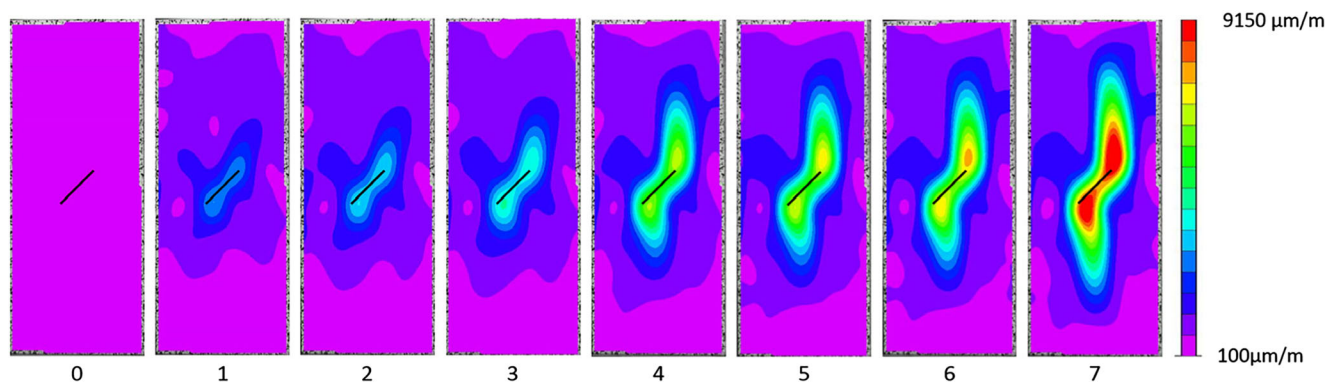


Fig. 6 Evolution of the strain field in a specimen with an inclination angle of 45°

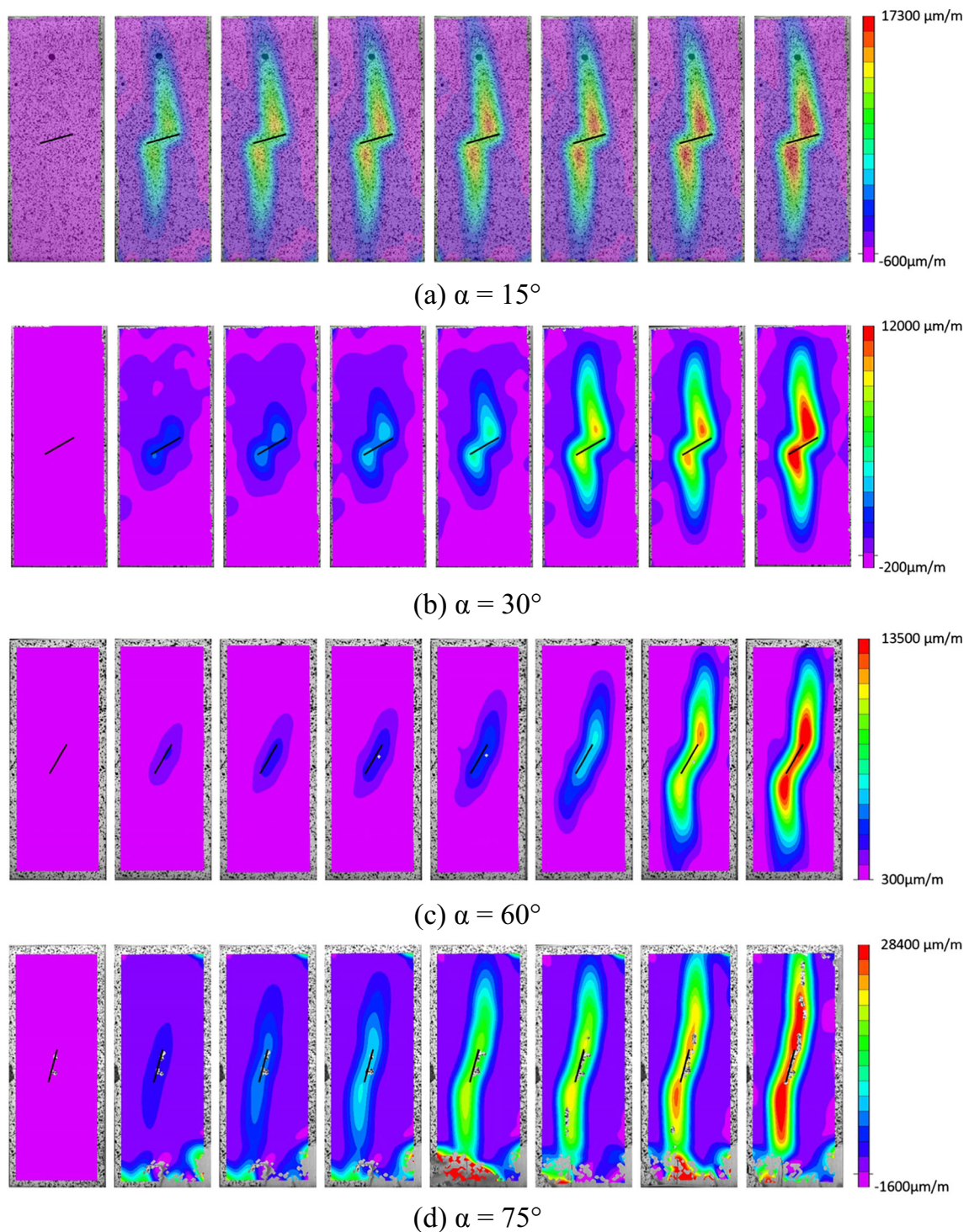


Fig. 7 Evolution of the strain fields in specimens with inclination angles of 15°, 30°, 60°, and 75°

Horizontal displacement

Figure 8 gives the horizontal displacements on the surfaces of the specimens with flaws at different angles as they approached failure. The evolution of the horizontal displacement accompanied by crack propagation was clearly

observed, which allows for the mechanism of crack propagation to be visualized. For example, as the flaw angle increased, the location of the largest displacement surrounding the flaw changed. The largest displacement was not always generated near the midpoint of the flaw but changed with the inclination angle.

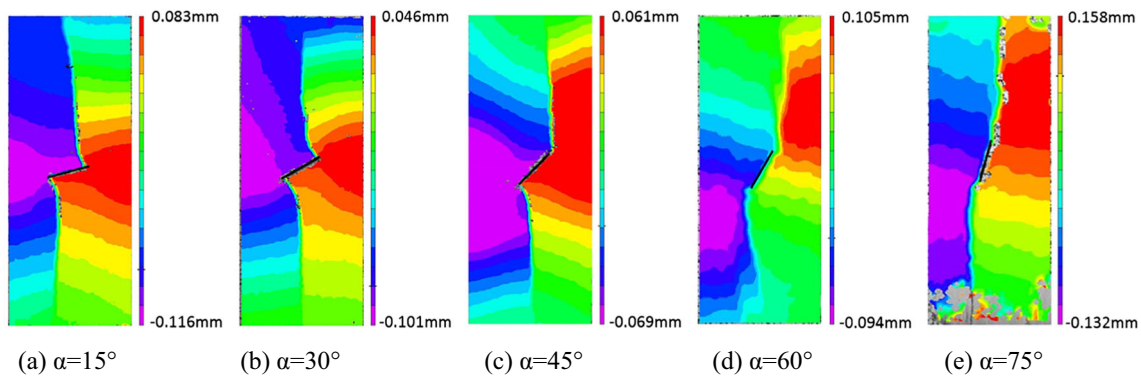


Fig. 8 Displacement fields in specimens with inclination angles of 15°, 30°, 60°, and 75°

When specimens were near failure, the horizontal displacement around the flaw tips reached the maximum value. However, as the inclination angle increased, the larger horizontal displacement fields gradually shifted from the flaw tips to the upper and lower sides. The horizontal displacement field was symmetrically distributed on the left and right sides of the flaw when the inclination angle was 15° or 30°. The specimens mostly failed under tensile stress with wing cracks. The horizontal displacement field was anti-symmetrically distributed at the two ends of the flaw tips when the inclination angle was 60° or 75°. The specimens mostly failed under shear stress with secondary shear cracks. When the inclination angle was 45°, the distribution of the horizontal displacement field had both types of characteristics. The corresponding types of crack propagation and shape were also relatively complex and changeable.

Expanded distinct element method (EDEM)

In order to expand and quantify the experimental results with the DIC method, the failure process of a single-flaw specimen was numerically simulated by using the strain strength criterion with the EDEM. The crack propagation trajectories are able to be determined by setting up virtual cracks in all potential cracking areas. The mechanical properties of the rock-like specimens are simulated by both the virtual cracks and the blocks.

To describe tensile cracks and shear cracks comprehensively, this paper employs an independent strain strength criterion (Zhao et al. 2017); it contains a tensile crack judgment criterion based on the principal strain and a shear crack judgment criterion based on the Mohr–Coulomb criterion. One basic assumption of this criterion is the tensile crack expands in the direction of the maximum principal strain, and the tensile crack begins to expand when the principal strain reaches a critical value (ε_t). Another assumption is the shear crack expands in the direction of the most dangerous stress state,

and the shear crack begins to expand when the Mohr circle stress state exceeds the Mohr–Coulomb failure line. Two-crack judgment factors are defined as follows for the judgment of the tensile crack and shear crack in numerical simulation:

$$f_t = \sigma_3 - \nu\sigma_1 + E\varepsilon_t \quad (1)$$

$$f_s = \sigma_1 - \frac{1 + \sin\varphi}{1 - \sin\varphi} \sigma_3 - 2c \sqrt{\frac{1 + \sin\varphi}{1 - \sin\varphi}} \quad (2)$$

where c is cohesion; φ is the internal friction angle; ε_t is the critical tensile strain; σ_1 and σ_3 are the principal stresses in the crack tip region when the pressure is positive; f_t is the judgment factor for the tensile crack and when $f_t > 0$, the tensile crack initiates; and f_s is the judgment factor for the shear crack and when $f_s > 0$, the shear crack initiates. When the equivalent stress state of the virtual crack satisfies the strength criterion, the virtual cracks are given the material parameters of real cracks, and a new crack initiates (Zhao et al. 2018b). The calculated area was separated into multiple hexagonal blocks by a finite number of discontinuous planes. Thus, the blocks were in close proximity to crystal grains. The hexagonal blocks can be regarded as being composed of six triangular blocks, which not only provide diversity in the direction of crack propagation but also ensure the computational efficiency and accuracy of the model.

The numerical specimen had dimensions of 100 mm high and 40 mm wide (see Fig. 9) to match the experiment and was cut by virtual cracks. The side length of a hexagonal block was 1.5 mm. The block could deform to obtain the stress and strain inside it. After the hexagonal block was formatted, it was divided with a triangular mesh for which the maximum length of the grid was less than 1 mm. The vertical displacement at the bottom of the specimen was fixed, and the top surface was under the displacement load.

The characteristics of the crack propagation differed partly because of the different angles of the flaws. First, the stress–strain curves differed, which indicated that the stress of crack initiation and the peak strength were different. Second, the

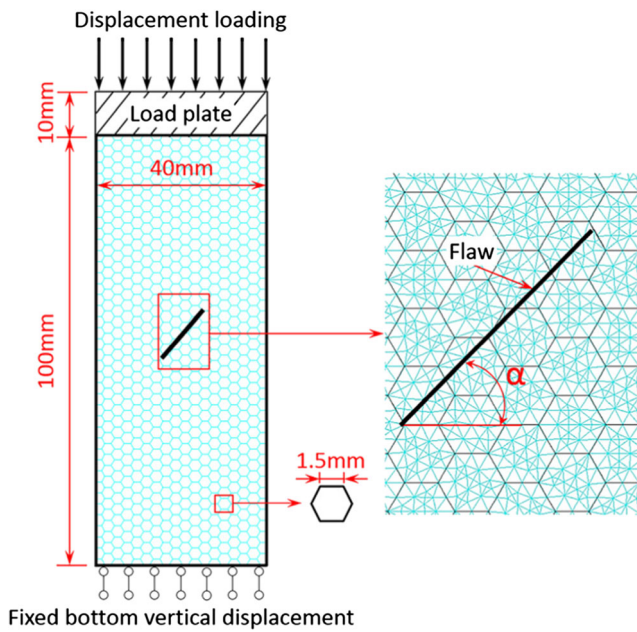


Fig. 9 Numerical model

propagation path differed, and the tensile and shear characteristics differed with crack evolution. The influence of the flaw angle on the failure mechanism of the specimen was studied in terms of the crack initiation, peak strength, crack propagation pattern, and tensile and shear characteristics.

Comparison of crack initiation and propagation

Figure 10a shows the stress–strain curves of specimens with flaws at different angles during the laboratory test. Figure 10b shows the quantified initiation stress and peak strength of the specimens during the laboratory test and the numerical simulation. The initiation stress was generally 70–90% of the peak strength. A larger ratio indicated more sudden crack propagation and more obvious brittle failure. The inclination angle affected not only the initiation stress but also the peak strength. The initiation stress and peak strength of the specimens decreased as the inclination angle increased from 15° to 60° and increased with the inclination angle from 60° to 75°. When the inclination angle was 60°, the initiation stress and peak strength were minimum, which indicated the stress concentration was highest and cracking was most likely to occur at the inclination angle of 60°.

Because the parameters were determined based on the peak strength of the specimen at an inclination angle of 45°, the strength of the specimen in the experiment was consistent with the numerical simulation, and the initiation stresses were generally equal. However, there were differences at other flaw angles between the laboratory test and numerical simulation that may be due to the difficulty of determining the microscopic parameters in the experiment. The numerical results were in good agreement with the

experimental results regarding the overall crack propagation process and the strength of specimens with different inclination angles.

Failure modes

Figure 11 shows the failure patterns of specimens with different inclination angles in the experiment and numerical simulation. The crack propagation paths for different inclination angles were basically the same: they started from the vicinity of the flaw tips, propagated to the upper and lower boundaries of the specimen along the loading direction, and finally coalesced throughout the specimen.

The crack propagation path was relatively curved in the experimental specimens, particularly at the beginning of the crack initiation, but the direction of the crack propagation in the numerical simulation was basically parallel to the loading direction in the middle and later stages. This is because the

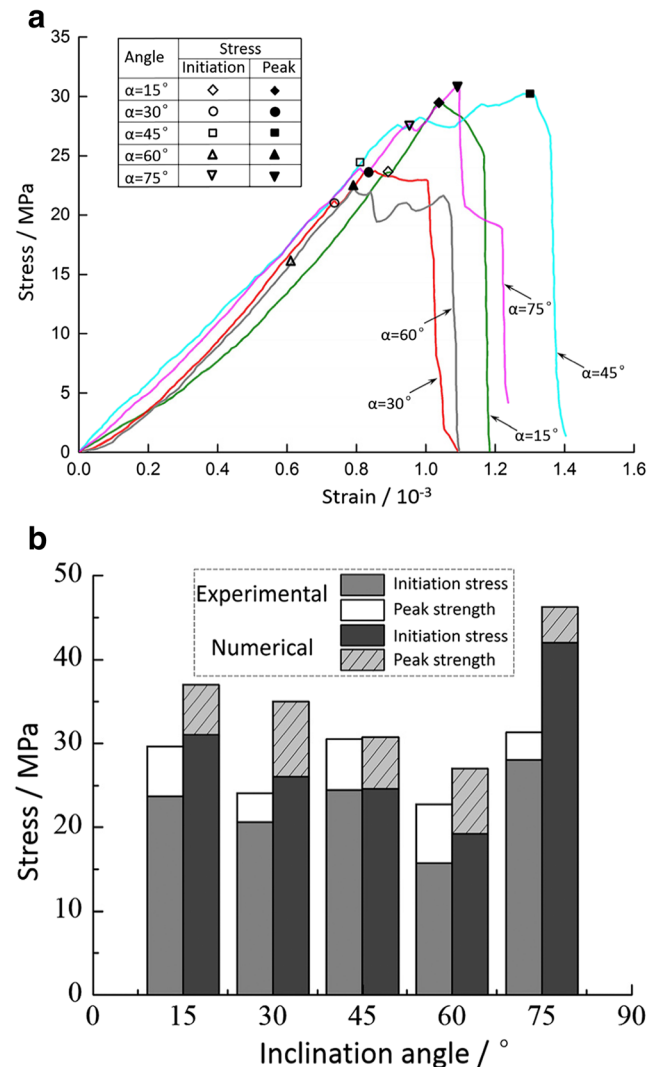
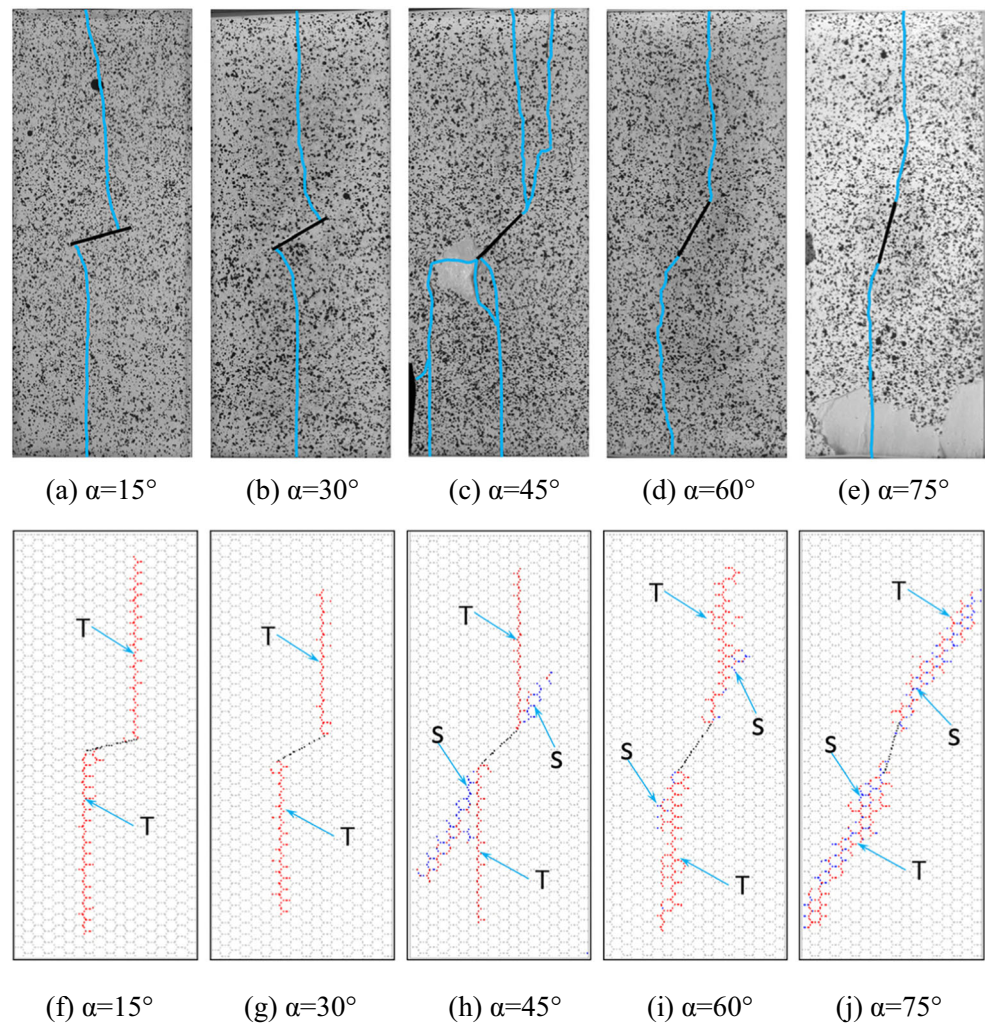


Fig. 10 a Stress–strain curves; b Initiation stress and peak strength

Fig. 11 Crack patterns and paths of specimens with different inclination angles in experimental study (a, b, c, d, and e) and numerical study (f, g, h, i, and j) (T for tensile crack, S for shear crack)



discrete element program used hexagonal blocks of the same size. The flaw tips were not so precise, so the crack propagation direction was limited. This is mainly because of the limitations of the program, which can be resolved by reducing the element size used in the numerical mode. The bending phenomenon of the cracks became less obvious when the inclination angle was larger. The crack propagation path in the specimen with an inclination angle of 75° was significantly different from that of the experimental result. This difference is because the numerical simulation showed obvious characteristics of shear failure, and the crack extended at both ends of the specimen along the 65° inclination direction.

When the inclination angle was small (15° and 30°), the crack propagation process was mainly tensile, and the shear cracks typically appeared after the peak strength. When the inclination angle was large (45° , 60° , and 75°), the specimens exhibited a mixture of tensile and shear characteristics. In the specimen with an inclination angle of 60° , a tensile crack was generated first at the flaw tips, and the shear cracks occurred shortly thereafter. The rate of tensile failure was larger than that of shear failure, and the macroscopic cracks showed a

mixture of tensile and shear characteristics. When the inclination angle was 75° , tensile and shear cracks were generated almost simultaneously and propagated at the same rate, and the process from initiation to failure was almost instantaneous.

Conclusions

In this study, the DIC method and EDEM were applied to examine the crack growth of rock-like specimens containing single flaws at different angles under uniaxial compression. This article analysed the effects of flaw angles in rock-like material to provide a better understanding of the failure mechanisms of geological engineering rock mass for predicting the unstable failure of jointed rock engineering. Based on the results, the following conclusions were obtained:

- (1) The principal strain field clearly changed around the flaw after loading. The principal strain concentration at the vicinity of the flaw tips indicated that the crack evolution entered the pre-initiation stage. The extension direction

of the principal strain field at the microscale was consistent with the direction of the crack propagation at the macroscale, which was parallel to the loading direction. The principal strain near the upper and lower boundaries clearly increased after the peak stress was reached, which indicates that the cracks were near coalescence and the specimens approached failure.

- (2) The position of the maximum principal strain concentration changed as the flaw angle increased from inside the flaw to the flaw tips. The positions with the largest horizontal displacement changed with the inclination angle when the specimen was near failure. The horizontal displacement field changed from a symmetric distribution to an anti-symmetric distribution as the inclination angle increased. Specimens mostly failed under tensile stress when the inclination angle was 15° or 30° and under shear stress when the inclination angle was 60° or 75°.
- (3) The initiation stress was generally 70–90% of the peak strength. Differently angled flaws affected the initiation stress and peak strength. They were both minimum when the flaw angle was 60°, which indicates that the stress was most concentrated, and cracking was most likely to occur when the flaw angle was 60°. The shear cracks usually appeared after the peak strength when the inclination angle was small (15° and 30°). The specimens exhibited a mixture of tensile and shear characteristics during loading when the inclination angle was large (45°, 60°, and 75°).

Acknowledgements The authors would like to acknowledge the financial support of the National Key Research and Development Plan [grant number 2017YFC0805004], National Natural Science Foundation of China [grant number 41202193, 41572262], and the Shanghai Rising-Star Program [grant number 17QC1400600].

References

- Agwai A, Guven I, Madenci E (2011) Predicting crack propagation with peridynamics: a comparative study. *Int J Fract* 171(1):65–78
- Ashby MF, Hallam SD (1986) The failure of brittle solids containing small cracks under compressive stress states. *Acta Metall* 34(3):497–510
- Basu A, Mishra DA, Roychowdhury K (2013) Rock failure modes under uniaxial compression, Brazilian, and point load tests. *Bull Eng Geol Environ* 72(3–4):457–475
- Bieniawski ZT (1967) Mechanism of brittle fracture of rock, part II—experimental studies. *Int J Rock Mech Min Sci* 4(4):407–423
- Bobet A, Einstein HH (1998) Fracture coalescence in rock-type materials under uniaxial and biaxial compression. *Int J Rock Mech Min Sci* 35(7):863–888
- Brace WF, Bombolakis EG (1963) A note on brittle crack growth in compression. *J Geophys Res* 68(12):3709–3713
- Cao P, Liu T, Pu C, Lin H (2015) Crack propagation and coalescence of brittle rock-like specimens with pre-existing cracks in compression. *Eng Geol* 187:113–121
- Chaker C, Barquins M (1996) Sliding effect on branch crack. *Phys Chem Earth* 21(4):319–323
- Cundall PA, Strack ODL (1979) A discrete numerical model for granular assemblies. *Geotechnique* 29(1):47–65
- Fan LF, Wu ZJ, Wan Z, Gao JW (2017) Experimental investigation of thermal effects on dynamic behavior of granite. *Appl Therm Eng* 125:94–103
- Gui YL, Bui HH, Kodikara J, Zhang QB, Zhao J, Rabczuk T (2016) Modelling the dynamic failure of brittle rocks using a hybrid continuum-discrete element method with a mixed-mode cohesive fracture model. *Int J Impact Eng* 87:146–155
- Gui YL, Zhao ZY, Zhang C, Ma SQ (2017) Numerical investigation of the opening effect on the mechanical behaviours in rocks under uniaxial loading using hybrid continuum-discrete element method. *Comput Geotech* 90:55–72
- Guo SF, Qi SW, Cai M (2016) Influence of tunnel wall roughness and localized stress concentrations on the initiation of brittle spalling. *Bull Eng Geol Environ* 75(4):1597–1607
- Hoek E, Bieniawski ZT (1965) Brittle fracture propagation in rock under compression. *Int J Fract* 1(3):137–155
- Horii H, Nemat-Nasser S (1985) Compression-induced microcrack growth in brittle solids: axial splitting and shear failure. *J Geophys Res* 90(B4):3105–3125
- Hu M, Liu Y, Ren J, Wu R, Zhang Y (2017) Laboratory test on crack development in mudstone under the action of dry-wet cycles. *Bull Eng Geol Environ* 2017(4):1–14
- Huang J, Chen G, Zhao Y, Wang R (1990) An experimental study of the strain field development prior to failure of a marble plate under compression. *Tectonophysics* 175(1):269–284
- Huang ML, Tang CA, Zhu W (2000) Numerical simulation on failure process of rock. *Chin J Rock Mech Eng* 19(4):468–471
- Jia CJ, Xu WY, Wang SS, Wang RB, Yu J (2018) Experimental analysis and modeling of the mechanical behavior of breccia lava in the dam foundation of the Baihetan hydropower project. *Bull Eng Geol Environ*. <https://doi.org/10.1007/s10064-018-1228-3>
- Jiang MJ, Chen H, Zhang N, Fang R (2014) Distinct element numerical analysis of crack evolution in rocks containing pre-existing double flaw. *Rock Soil Mech* 35(11):3259–3268
- Jiang Y, Li B, Yamashita Y (2009) Simulation of cracking near a large underground cavern in a discontinuous rock mass using the expanded distinct element method. *Int J Rock Mech Min Sci* 46(1):97–106
- Lin Q, Labuz JF (2013) Fracture of sandstone characterized by digital image correlation. *Int J Rock Mech Min Sci* 60:235–245
- Liang CY, Zhang QB, Li X, Xin P (2016) The effect of specimen shape and strain rate on uniaxial compressive behavior of rock material. *Bull Eng Geol Environ* 75(4):1669–1681
- Morgan SP, Johnson CA, Einstein HH (2013) Cracking processes in Barre granite-fracture process zones and crack coalescence. *Int J Fract* 180(2):177–204
- Petit J, Barquins M (1988) Can natural faults propagate under mode II conditions? *Tectonics* 7(6):1243–1256
- Reyes O, Einstein HH (1991) Failure mechanisms of fractured rock—a fracture coalescence model. *Proc seventh Int Congr. Rock Mech* 1:333–340
- Sagong M, Bobet A (2002) Coalescence of multiple flaws in a rock-model material in uniaxial compression. *Int J Rock Mech Min Sci* 39(2):229–241
- Shen B, Stephansson O, Einstein HH, Ghahreman B (1995) Coalescence of fractures under shear stress experiments. *J Geophys Res* 100(B4):5975–5990
- Tang CA, Lin P, Wong RHC, Chau KT (2001) Analysis of crack coalescence in rock-like materials containing three flaws—part II: numerical approach. *Int J Rock Mech Min Sci* 38(7):925–939
- Tarokh A, Blanksma DJ, Fakhimi A, Labuz JF (2016) Fracture initiation in cavity expansion of rock. *Int J Rock Mech Min Sci* 85:84–91

- Vesga LF, Vallejo LE, Lobo-Guerrero S (2008) DEM analysis of the crack propagation in brittle clays under uniaxial compression tests. *Int J Numer Anal Met* 32(11):1405–1415
- Wong LNY, Einstein HH (2006) Fracturing behavior of prismatic specimens containing single flaws. In: *Proceedings of the 41st US symposium on rock mechanics*, 17–21 June 2006, Golden, Colorado
- Wong LNY, Einstein HH (2009a) Crack coalescence in molded gypsum and Carrara marble: part 1. Macroscopic observations and interpretation. *Rock Mech Rock Eng* 42:475–511
- Wong LNY, Einstein HH (2009b) Crack coalescence in molded gypsum and Carrara marble: part 2. Microscopic observations and interpretation. *Rock Mech Rock Eng* 42:513–545
- Wong RHC, Chau KT (1998) Crack coalescence in a rock-like material containing two cracks. *Int J Rock Mech Min Sci* 35(2):147–164
- Wong RHC, Chau KT, Tang CA, Lin P (2001) Analysis of crack coalescence in rock-like materials containing three flaws—part I: experimental approach. *Int J Rock Mech Min Sci* 38(7):909–924
- Wu ZJ, Fan LF, Liu QS, Ma GW (2017) Micro-mechanical modeling of the macro-mechanical response and fracture behavior of rock using the numerical manifold method. *Eng Geol* 225:49–60
- Wu ZJ, Wong LNY (2013) Modeling cracking behavior of rock mass containing inclusions using the enriched numerical manifold method. *Eng Geol* 162:1–13
- Yang SQ, Huang YH, Tian WL, Zhu JB (2017) An experimental investigation on strength, deformation and crack evolution behavior of sandstone containing two oval flaws under uniaxial compression. *Eng Geol* 217:35–48
- Yang SQ, Jing HW (2011) Strength failure and crack coalescence behavior of brittle sandstone samples containing a single fissure under uniaxial compression. *Int J Fract* 168(2):227–250
- Yang SQ, Tian WL, Huang YH, Ranjith PG, Ju Y (2016) An experimental and numerical study on cracking behavior of brittle sandstone containing two non-coplanar fissures under uniaxial compression. *Rock Mech Rock Eng* 49(4):1497–1515
- Zhang XP, Wong LNY (2012) Cracking processes in rock-like material containing a single flaw under uniaxial compression: a numerical study based on parallel bonded-particle model approach. *Rock Mech Rock Eng* 45(5):711–737
- Zhang XP, Wong LNY (2014) Displacement field analysis for cracking processes in bonded-particle model. *Bull Eng Geol Environ* 73(1):13–21
- Zhang XP, Wong LNY, Wang S (2015) Effects of the ratio of flaw size to specimen size on cracking behavior. *Bull Eng Geol Environ* 74(1):181–193
- Zhao C, Ma CC, Zhao CF, Du SG, Bao C (2017) Crack propagation simulation of rock-like specimen using strain criterion. *Eur J Environ Civ Eng*. <https://doi.org/10.1080/19648189.2017.1359677>
- Zhao C, Matsuda H, Lou S, Guan ZC, Tian JS (2013) Visualization of buckling on thin-walled cylindrical shell by digital image correlation method. *Appl Math Inform Sci* 7(3):999–1004
- Zhao C, Niu JL, Zhang QZ, Zhao CF, Xie JF (2018a) Buckling behavior of a thin-walled cylinder shell with the cutout imperfections. *Mech Adv Mater Struct*. <https://doi.org/10.1080/15376494.2018.1444225>
- Zhao C, Zhou YM, Zhao CF, Bao C (2018b) Cracking processes and coalescence modes in rock-like specimens with two parallel pre-existing cracks. *Rock Mech Rock Eng*. <https://doi.org/10.1007/s00603-018-1525-y>
- Zhao F, He MC (2017) Size effects on granite behavior under unloading rockburst test. *Bull Eng Geol Environ* 76(3):1183–1197
- Zheng Y, Chen CX, Liu TT, Zhang W, Song YF (2018) Slope failure mechanisms in dipping interbedded sandstone and mudstone revealed by model testing and distinct-element analysis. *Bull Eng Geol Environ* 77(1):49–68
- Zou C, Wong LNY (2014) Experimental studies on cracking processes and failure in marble under dynamic loading. *Eng Geol* 173:19–31